MIT Libraries | DSpace@MIT

MIT Open Access Articles

Heterogeneous Nucleation of an n-Alkane on Tetrahedrally Coordinated Crystals

Massachusetts Institute of Technology

Heterogeneous Nucleation of an n-Alkane on Tetrahedrally Coordinated Crystals

Alexander J. Bourque[a], C. Rebecca Locker[b], Gregory C. Rutledge[a*]

[a]Department of Chemical Engineering, Massachusetts Institute of Technology,

Cambridge, MA 02139

[b]ExxonMobil Research and Engineering Company, Annandale NJ 08801

[*]Corresponding author. Tel.: +1 617 253 0171; fax: +1 617 258 5766.

E-mail address: rutledge@mit.edu (G. C. Rutledge).

Abstract

Heterogeneous nucleation refers to the propensity for phase transformations to initiate preferentially on foreign surfaces, such as vessel walls, dust particles or formulation additives. In crystallization, the form of the initial nucleus has ramifications for the crystallographic form, morphology and properties of the resulting solid. Nevertheless, the discovery and design of nucleating agents remains a matter of trial and error, due to the very small spatio-temporal scales over which formation of the critical nucleus occurs, and the extreme difficulty of examining such events empirically. Using molecular dynamics simulations, we demonstrate a method for the rapid screening of entire families of materials for activity as nucleating agents, and for characterizing their mechanism of action. The method is applied to the crystallization of n-pentacontane, a model surrogate for polyethylene, on the family of tetrahedrally coordinated crystals including diamond and silicon. Systematic variation of parameters in the interaction potential permits a comprehensive, physically-based screening of nucleating agents in this class of materials, including both real and hypothetical candidates. The induction time for heterogeneous nucleation is shown to depend strongly on crystallographic registry between the nucleating agent and the critical nucleus, indicative of an epitaxial mechanism in this class of materials. Importantly, the severity of this registry requirement weakens with decreasing rigidity of the substrate and increasing strength of attraction to the nucleating agent surface. Employing this method, high throughput computational screening of nucleating agents becomes possible, facilitating the discovery of novel nucleating agents within a broad, "materials genome" of possible additives.

Introduction

Phase change, whether condensation of liquid from vapor, precipitation from solution or crystallization of a solid from the melt, generally occurs through a two-stage process of nucleation and growth of the new phase within the old one. The nucleation step is an activated process that relies on microscopic fluctuations to produce a critically sized nucleus of the new phase. A typical critical nucleation event might involve a cluster of only a few 100's or 1000's of atoms that fluctuates into existence in a matter of nanoseconds, making it impossible to reliably detect in experiment. Fortunately, nearly instantaneous growth of the nucleus to detectable sizes permits estimation of the induction time, which is rigorously defined as the time to reach a critical nucleus size. Experimental measurements of induction times and theoretical predictions of nucleation processes have been well reviewed in numerous texts, e.g, Oxtoby,[1,2] Debenedetti[3] and Kashchiev,[4] yet the persistent inability to observe critical and sub-critical nuclei in experiments has left deficiencies in our understanding of nucleation phenomena. Furthermore, attention in the literature is devoted predominantly to homogeneous nucleation, or the formation of nuclei within a relatively pure phase of the material. Heterogeneous nucleation, or the formation of a nucleus of the new phase on the surface of a foreign material, is often ignored, despite its importance as the more common mechanism for first-order phase transitions. The propensity for heterogeneous nucleation is driven by the ubiquity of foreign material in practical settings, either as impurities (dust, catalyst residue, etc.), vessel walls or formulation additives. Hence, at a given supersaturation condition, heterogeneous nucleation usually proceeds orders of

magnitude faster than homogeneous nucleation such that the distribution of nuclei strongly favors the former.

Control of nucleation is essential in crystallization processes because so many important properties of the resulting solid material are determined by nucleation. Examples of nucleation-controlled properties include polymorph selection[5] and crystallite size distributions[6] in pharmaceuticals, quality of solution-crystallized proteins[7,8] and a number of material properties in semicrystalline polymers.[9] An effective means to control nucleation is to introduce nucleating agents into a supersaturated solution or melt. Nucleating agents are defined as any foreign matter that promotes heterogeneous nucleation. Good nucleating agents are those that greatly increase the rate of nucleation while promoting desired crystal morphologies over uncontrolled crystal phases that may otherwise nucleate on random solid impurities in solution or in the melt. Experimental studies of nucleating agents have led to some common heuristics for the selection of good nucleating agents for pharmaceuticals,[10] polymers[11-14] and most recently proteins.[15,16] These studies identified characteristics that enhance nucleation, including compatible polarity and crystallographic matching between the nucleating agent and the crystallite. These findings are, however, based upon indirect evidence, such as the macroscopic characterization of the crystallized morphologies rather than direct observations of nucleation.

Advances in computer simulation have opened up new avenues to study nucleation. In general, Monte Carlo methods provide a means to identify the critical nucleus and to

quantify the free energy barrier to nucleation, within a kinetic theory of nucleation,[17-19]

provided one can identify a suitable reaction coordinate along which the nucleation

barrier resides. In some cases, molecular dynamics (MD) simulations have been used to

observe the structure and kinetics of formation of nuclei directly, albeit *in silico,* without

prior knowledge of the reaction coordinate. Successful MD simulations of homogeneous

nucleation have been observed in a LJ fluid,[20] water,[21] *n*-alkanes[22,23] and polymers.[24] In

the few cases where computer simulations were used to study heterogeneous nucleation,

usually only specific combinations of material and surface were considered.[25-32] Among

these, a few studies manipulated the surface forces to probe the effects of

hydrophobicity.[30-32] Of particular relevance to the current approach are the works of

Reinhardt and Doye,[33] and of Fitzner et al.[34], both of which examined the nucleation of

ice on a variety of static surfaces by varying either the lattice constants or the nature of

interaction of the surface with the water molecules. For crystallization of chain-like

molecules, the most relevant study is one in which propagation of the crystal growth front

was characterized in terms of surface nucleation and spreading within successive layers

of a crystallizing n-alkane.[26] Critical nucleus sizes, induction times, and rates for surface

nucleation were estimated and used to parameterize a new kinetic model for

crystallization in chain molecules.[35]

In this work, we demonstrate the utility of MD simulation for screening systematically

the activity of nucleating agents, and for characterizing their mechanism of action. As

nucleating agents, we examine the entire family of tetrahedrally coordinated crystals

described by the Stillinger-Weber (SW) potential.[36] Familiar members of this family

include diamond-like materials such as silicon, diamond and germanium, as well as binary zincblende compositions such as ZnS, GaAs and SiC. In typical applications, the parameters of the SW potential are tuned to reproduce the physical properties of a specific material.[36-38] Here, we vary the parameters of the SW potential to represent a continuous composition space that includes both real and hypothetical materials. Using the SW potential, a tetrahedrally coordinated nucleating agent is uniquely identified by four parameters: a length scale (the atomic diameter, σ_{SW}), a cohesive energy scale (the depth of the two-body interaction potential, ε_{SW}), a tetrahedral strength (the relative strength λ_{SW} of the three-body interaction contributions that determines the rigidity of the tetrahedral structure) and an adhesive energy scale (the depth ε_{AD} of the interaction potential between the nucleating agent and the crystallizing material). In this study, we investigate the effect of lattice spacing, structural rigidity and adhesive interaction strength on crystallization of n-pentacontane ($C_{50}H_{102}$ or C50), a model analogue for polyethylene. In contrast to previous studies,[33,34] the nucleating agent is dynamic and fully thermalized, with important consequences.

Methods

C50 chains were modeled using the united atom (UA) force field developed by Paul, Yoon and Smith (PYS)[39] and subsequently modified by Waheed et al.[40,41] C50 crystallizes in a hexagonal, rotator phase with this force field, so that different growth directions in the organic phase (e.g. [100], [010], [110]) are essentially equivalent. The intramolecular interactions of the nucleating agents were represented by the Stillinger-Weber (SW) potential.[36] The values $A = 7.049556277$, $B = 0.602224558$, $p = 4$, $q = 0$, $\gamma =$

1.2, $a = 1.8$ and $\theta_o = 109.5°$ were fixed, while σ_{SW}, ε_{SW} and λ_{SW} were varied in this work. These intramolecular parameters were bounded such that the tetrahedral state was the equilibrium state for the nucleating agent during both melt equilibration ($T = 550$ K) and quenching ($T = 360$ K). Adhesive interactions between the organic C50 and nucleating agent were represented with a pairwise Lennard-Jones potential,

$$E_{AD} = 4\varepsilon_{AD}\left[\left(\frac{\sigma_{AD}}{r}\right)^{12} - \left(\frac{\sigma_{AD}}{r}\right)^{6}\right] \tag{1}$$

where σ_{AD} was set equal to $\sigma_{PP} = 0.4$ nm, the interaction distance between CH_2 beads in the PYS force field. The interaction parameter ε_{AD} was also varied in this work.

Molecular dynamics simulations were performed using the LAMMPS software package.[42] All results are presented for simulations in an NPT ensemble with pressure $P = 1$ atm. The barostat and thermostat were both of the Nosé-Hoover type, with damping frequencies $\omega_P = 1/(1000$ fs$)$ and $\omega_T = 1/(10$ fs$)$, respectively. Atomic forces were integrated using the rRESPA multiple time step integrator, with a time step of 2.5 fs for bond length, angle and dihedral interactions, and 5 fs for all pairwise interactions. An orthorhombic simulation box was used for all simulations; the side lengths were allowed to vary independently, and periodic boundary conditions were applied in all three directions. Three hundred fully-extended C50 chains were initially arranged in 20 layers of 15 chains. The nucleating agent was represented by $N_x \times N_y \times N_z$ repetitions of its crystal unit cell of lattice dimension $l_x \times l_y \times l_z$ with the desired (hkl) plane in contact with the n-alkane phase. N_x and N_y were chosen to span the initial n-alkane phase in the xy-plane and N_z was chosen large enough to account fully for intermolecular interactions

with the *n*-alkane phase (Lennard-Jones cutoff distance = 1 nm) without interactions

between the two surfaces. The substrate area in contact with the *n*-alkane phase was $A =$

50 ± 2 nm^2.

All simulations were run in the isothermal-isobaric (NPT) ensemble. The system was

equilibrated at 550 K, above the melting point ($T_m = 370$ K) of the organic but below the

melting point of the nucleating agent. The initial melt density was 0.71 g/cm^3, which is

comparable to the melt density of similar n-alkanes near this temperature.[43] Periodic

boundary conditions were used in all three directions, resulting in two crystal/liquid

interfaces. Averages were taken over four independent configurations for each nucleating

agent tested, for a total sample of eight nucleation events; although small, this sample

size is sufficient to distinguish good nucleating agents from bad ones, for screening

purposes. At time $t = 0$ ns, simulations were quenched to the crystallization temperature

$T_c = 360$ K, a supercooling of $\Delta T/T_m = 3\%$, to induce crystallization of the C50 chains.

This T_c was chosen to because it results in the fastest rate of crystallization for C50.[26]

A local orientational order parameter $p_2 = \left(3\left\langle \cos^2 \theta_{ij} \right\rangle - 1\right)\big/2$ was used to track the

crystallinity, where θ_{ij} is the angle between the vectors joining the nearest neighbor UA

beads of sites i and j, respectively. The average is taken over all of the neighboring UA

beads j that lie within a LJ cutoff distance $r_{ij} < 2.5$ σ_{PP} of the *i*th UA bead.[23] To analyze

crystal growth, the *n*-alkane domain was divided into slices of thickness 0.4 nm,

comparable to the thickness of a single layer of chain segments in the C50 crystal, taken

normal (*xy*-plane) to the growth direction (*z*). The outermost layer(s) of SW sites were

used to define $z = 0$ at the surface(s) of the nucleation agent. The number of crystalline

beads $N_c(z)$ in a given slice was measured as a function of time using the criteria, $p_2(i) >$

0.4. Clusters of crystallized UA beads were identified within each slice according to a 2D

clustering algorithm: bead j was assigned to a cluster containing bead i if the following

three criteria were met: $p_2(j) > 0.4$, $r_{ij} < 1.3\sigma_{PP}$, and beads i and j belong to the same slice.

The fractional crystallinity $X(z)$ of a slice was calculated as the total number of crystalline

beads in a given slice $N_c(z)$ divided by the total number of beads within the slice $N_T(z)$:

$X(z) = N_c(z)/N_T(z)$. The displacement D of the crystal/melt interface in the C50 domain

from $z = 0$ was identified using a Gibbs dividing surface based on the fractional

crystallinity:[26]

$$\Delta X_{c,\text{int}} = \int_{-\infty}^{\infty}\left[H(z-D) - X(z)\right]dz = 0, \tag{2}$$

where $H(x)$ is the Heaviside function. Simulations were continued as long as there was a

0.4 nm slice between the displaced interfaces where $X(z) < 0.2$, so that the two interfaces

did not influence one another.

Silicon ($\sigma_{SW} = 0.2095$ nm, $\varepsilon_{SW} = 209$ kJ/mol, $\lambda_{SW} = 21$) was used as a reference material

for the nucleating agent throughout this study. SW parameters are hereby defined with

reference to the values for silicon: $\sigma_{SW}^* = \sigma_{SW}/\sigma_{Si}$, $\varepsilon_{SW}^* = \varepsilon_{SW}/\varepsilon_{Si}$, $\lambda_{SW}^* = \lambda_{SW}/\lambda_{Si}$.

Similarly, the relative adhesive strength is defined as $\varepsilon_{AD}^* = \varepsilon_{AD}/\varepsilon_{PP}$, using ε_{PP}, the

polymer-polymer LJ interaction strength, as the reference.

Results and Discussion

The advancement of the C50 crystal growth front from the surface of a nucleating agent that is structurally identical to silicon, yet with an augmented adhesive strength, is shown in Figure 1(a) for a single simulation trajectory. In this representative example, there was little displacement of the crystal-amorphous interface before 130 ns. Afterwards, the growth front proceeded inwards more rapidly; by 150 ns, the chains were highly ordered ($X(z) > 0.8$) on the crystal side. Snapshots of the C50 crystal growing on the surface of the nucleating agent are illustrated in Figure 1(b)-(g). Densification and ordering of the C50 chains were observed near the organic-nucleating agent interface, with the axes of the crystallized chains aligned with the y-axis. The apparent gap in crystalline beads parallel to the x-axis in the MD snapshots at t = 200 ns is due to disorder arising from thermal motion of the C50 chain ends. Observations of the system at even longer times confirmed that the crystallites contained fully extended chains and that even the chain ends eventually crystallized, such that $X(z) \sim 1$ for all z at sufficiently long times.
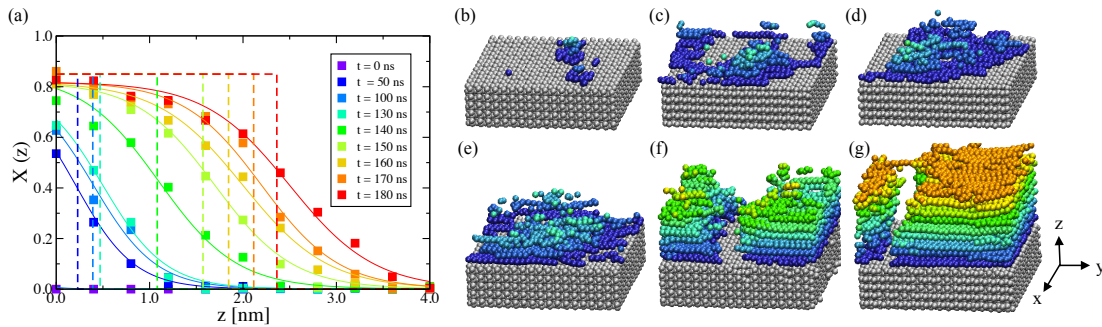

Figure 1.(a) Profiles of fractional crystallinity, $X(z)$, in the simulation box at various times following a quench to 360 K, for a single surface. The nucleating agent surface was the (110) crystal plane of silicon ($\sigma_{SW}^* = 1$, $\varepsilon_{SW}^* = 1$, $\lambda_{SW}^* = 1$) with an augmented adhesive strength ($\varepsilon_{AD}^* = 1.5$). The solid curves are linear least squares fits of hyperbolic tangent functions to the fractional crystallinity profiles. Dotted lines identify the locations of the

Gibbs dividing surface for the crystal/melt interfaces. Snapshots from MD simulation are provided for the times corresponding to (b) 5, (c) 25, (d) 50, (e) 100, (f) 150, (g) 200 ns. Only the nucleating agent (gray) and the crystallized C50 beads are shown, with each layer of crystallized C50 beads distinguished by a different color; C50 beads in the amorphous melt are not shown.

Figure 2 shows trajectories from 4 independent simulations for the displacement D of the crystal/melt interface as functions of time, for the same conditions as in Figure 1(a). Each displacement profile is characterized by two features. First, there is an induction period, in which the C50 chains order close to the surface of the nucleating agent. In this period, D increases to 0.5-0.7 nm for $\varepsilon_{AD}^* = 1.5$, shown in Figure 2, and then appears to saturate. The saturation threshold for D was found to be lower for weaker values of ε_{AD}^*. Second, the induction period is followed by a period of rapid crystal growth with constant growth rate G. Values of G were obtained from linear fits to trajectory data in the growth regime ($D \geq 0.8$ nm), and the induction time τ was defined by extrapolation of this line to $D = 0$. The growth rate and induction time averaged over all 8 displacement trajectories in Figure 2 is $G = 0.029 \pm 0.002$ nm/ns and $\tau = 62 \pm 15$ ns, respectively. Compared to our previous simulations of surface nucleation of C50 on an ideal, crystalline PE surface,[26] the growth rate G is similar in magnitude but the induction time is significantly longer than that of the crystalline PE surface ($\tau = 5$ ns). Thus, the induction time is characteristic of the nucleating agent and the material that crystallizes, whereas the growth rate is characteristic of the crystallizing material alone.
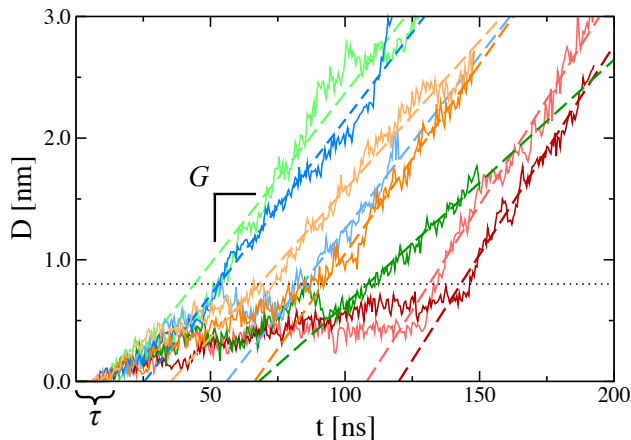
Figure 2. Displacement D of the crystal-melt interface in C50 from the (110) crystal plane of the nucleating agent (same parameters as Figure 1). Results are shown for 4 simulations, each represented by a different color (orange, green, blue, red), with 2 surfaces per simulation indicated by light and dark hues, for a total of 8 displacement trajectories. Dashed lines are linear fits to the trajectories in the region of steady-state crystal growth (above $D = 0.8$ nm, indicated by the horizontal dotted line). The slope of each dashed line is the growth rate G. Intersection of the dashed line with the time axis gives the induction time τ required to reach steady-state growth.

The analysis of heterogeneous nucleation employed here is analogous to the "direct observation method" (DOM) for evaluating homogeneous nucleation rates.[44,45] In the DOM, the homogeneous nucleation rate $i_{homo}=(\tau V)^{-1}$ is determined from the onset time τ required for the largest cluster within a volume V to exceed a threshold size. For heterogeneous nucleation we define the characteristic rate $i_{hetero} = (\tau A)^{-1}$, where τ is the induction time required for the crystal growth front to advance past a threshold distance from the surface of the nucleating agent of area A. This characteristic rate is an accurate

12

measure of the heterogeneous nucleation rate in the limit that there exists only one cluster at the growth front. Further discussion of surface nucleation rates and the relation to the mechanism of surface nucleation and crystal growth is presented in earlier work.[26,35]

Crystalline nucleating agents possess a variety of low index lattice planes that can serve as distinct surfaces for nucleation and growth of crystallites within the surrounding liquid. Figure 3 shows the induction time to steady-state growth τ, and the corresponding growth rate G, as functions of the adhesive strength, ε_{AD}^*, for the most important lattice planes of the tetrahedrally coordinated nucleating agents: (100), (110) and (111). The induction time was found to depend on the adhesive interaction strength and the crystal lattice plane of the nucleating agent. Induction times decreased steeply with a linear increase in ε_{AD}^*, regardless of which crystal plane was chosen for presentation to the melt. In this work, no nucleation events were observed within 600 ns of simulation time at the weakest adhesive strength considered, $\varepsilon_{AD}^* = 0.5$, while nucleation was observed only on the (110) plane for $\varepsilon_{AD}^* = 1.0$. At still higher adhesive strengths, the induction times plateaued to different values for nucleation from each crystal plane. These results accord with the results of Lupi et al[30] where interaction strength between the material (water) and the surface (graphite) was tuned homogeneously. They are also consistent with expectations from classical nucleation theory (CNT) in the capillary approximation;[3,46] in this case, reduction of the nucleation barrier is attributed to the relatively low interfacial energy of the material with the substrate, characterized by the contact angle, which results in a smaller critical nucleus size. The decrease in induction time with increasing adhesive strength demonstrates that adhesive interaction strength plays a significant role in

facilitating heterogeneous nucleation, and is consistent with low interfacial energy and small contact angle. However, the differences in induction times for the three crystallographic facets even at high adhesive strengths indicates additional contributions from other, crystallographic factors. Finally, Figure 3(b) demonstrates that whenever growth was observed, G did not vary strongly with $\varepsilon_{AD}{}^*$ or with exposed crystal facet. The invariance in the crystal growth rate indicates that the action of the nucleating agent is local, and affects only the induction time.
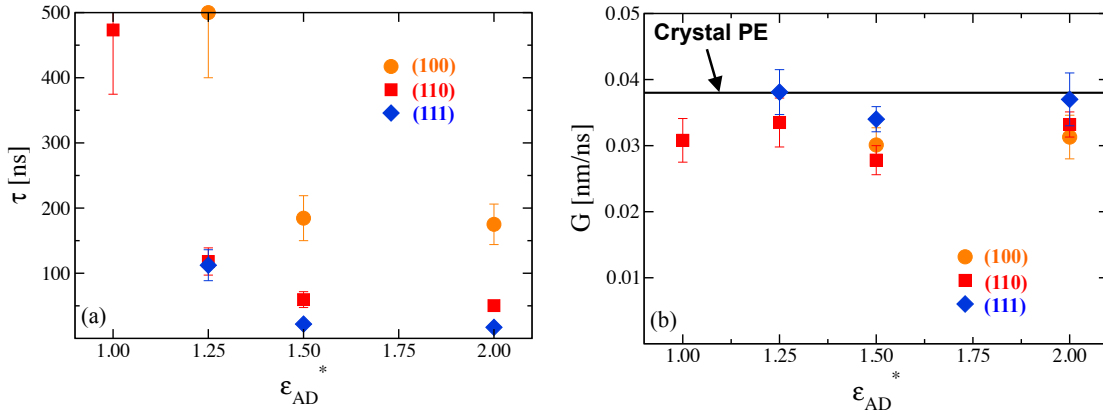

Figure 3. (a) Induction time to steady-state crystal growth, τ, in C50 as a function of the relative interaction strength, $\varepsilon_{AD}{}^*$. (b) The corresponding steady-state growth rates G in the "far from surface" regime. The growth rate of C50 observed from the crystalline PE (110) surface is included for reference.[26]

The alignment of crystallized chains at the nucleating agent surface is shown in Figure 4. Overlay with the respective crystal planes of the substrate – (100), (110) and (111) – confirms that the crystallized C50 chains are in registry with the underlying, crystallographic planes. Such alignment is consistent with the mechanism of epitaxial

14

matching between the polymer and the nucleating agent. The Mercury software package[47] was used to calculate the important d-spacings of the nucleating agent and their corresponding crystallographic directions. The d-spacings and crystallographic directions consistent with the C50 chain directions shown in Figure 4 are given in Table 1. Epitaxial matching was quantified by the parameter $\Delta = 100(d_p - d_s)/d_s$ where d_p and d_s are the matching distances of the n-alkane and substrate.[48] The matching distance for C50 is the spacing between chains, quantified as the lattice parameter $b = 0.49$ nm for the force field used in this work. According to Wittman and Lotz, the acceptable range of lattice mismatch for which epitaxy may be considered relevant is $|\Delta| \leq 15$ %.[11] Applying this condition, only the (110) crystal plane presents an epitaxial match for C50, $\Delta \sim 10\%$. This condition, however, is simply a heuristic and clearly fails to account for the performance of the (111) plane under conditions of high surface adhesion ($\varepsilon_{AD}^{*} > 1.25$). An epitaxial match, Δ, approaching -50% signifies a 3:2 ratio between the periodicity of the underlying substrate and the n-alkane unit cell, which may account for the short induction times atop the (111) plane. This alternative mechanism appears inactive when the attractive forces are weak.
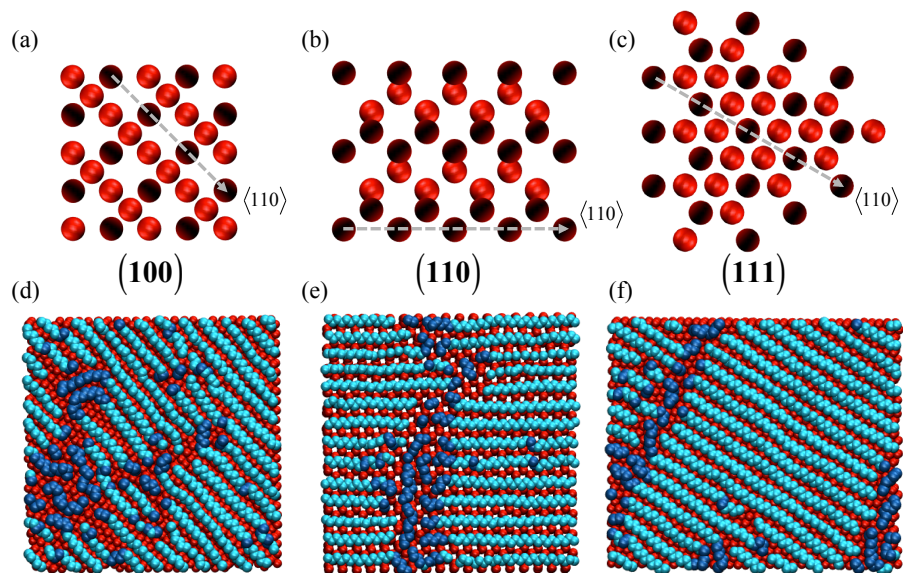
Figure 4. (a-c) Representative cuts of the tetrahedrally coordinated crystal lattice, showing the arrangement of surface and sub-surface sites for the low index crystallographic planes of Si: (a) (100), (b) (110) and (c) (111). The black sites constitute the plane at the silicon surface, while the red sites are sub-surface. (d-f) Snapshots of C50 beads within the first layer adjacent to the surface of the nucleating agent, taken from MD simulations at long times (t > 200 ns): (d) (100), (e) (110) and (f) (111). Crystalline UA beads are colored light blue, to distinguish them from noncrystalline UA beads (dark blue) and the sites belonging to the nucleating agent (red). The lines drawn in (a-c) show the crystallographic directions, <hkl>, that match the alignment of crystallized chains in (d-f).

Table 1. Crystallization from (100), (110) and (111) facets of the nucleating agent.

Crystal plane	τ [ns][a]	G [nm/ns][a]	Nucleus alignment	d_{hkl} [nm]	Δ
(100)	185 ± 35	0.030 ± 0.003	$<110>_{SW}$	0.384	- 27.6%

(110)	62 ± 15	0.029 ± 0.002	$<110>_{SW}$	0.543	$+ 9.8\%$
(111)	22 ± 4	0.034 ± 0.002	$<110>_{SW}$	0.332	$- 47.6\%$

[a] Results obtained for $\varepsilon_{SW}^{*} = 1$, $\sigma_{SW}^{*} = 1$, $\lambda_{SW}^{*} = 1$, $\varepsilon_{AD}^{*} = 1.5$

Figure 5 presents sections from a comprehensive mapping of the induction time over a three-dimensional parameter space for the nucleating agent that includes variations in σ_{SW}^{*}, λ_{SW}^{*} and ε_{AD}^{*}. This multidimensional parameter space constitutes a "materials genome" for tetrahedrally coordinated nucleating agents. The mapping was performed with the (110) interface of the nucleating agent in contact with the organic phase. The contrast in Figure 5(a)-(c) reaffirms that increasing *adhesive strength* results in a shift toward shorter induction times. Each section shown in Figure 5 furthermore demonstrates that matching the lattice periodicity of the nucleating agent with the periodicity of the *n*-alkane unit cell significantly reduces induction time. This is evidenced by a minimum in the induction time around $\sigma_{SW}^{*} = 0.9$ or $\Delta \sim 0$. The reduction in τ confirms the importance of *epitaxial matching* for heterogeneous nucleation in this class of materials. It is worth noting that the mapping was performed with significantly weaker adhesive forces than that used in Figure 3. Strong adhesive forces ($\varepsilon_{AD}^{*} \geq 1$) were required to achieve nucleation in a reasonable simulation time scale (t < 400 ns) when the substrate exhibited the periodicity of silicon ($\sigma_{SW}^{*} = 1$). In Figure 5, a sizable reduction in the induction time is achieved by reducing $\sigma_{SW}^{*} < 1$, even with weaker adhesive forces ($\varepsilon_{AD}^{*} \leq 1$). This particular result underscores the significant impact lattice matching has on the nucleation rate.

Remarkably, the effect of crystal mismatch was found to be less severe when the structural rigidity of the nucleating agent, λ_{SW}, was decreased from its reference value, λ_{Si}. This observation reveals, apparently for the first time, that the *rigidity* of the nucleating agent can affect the formation of stable nuclei. For lower values of λ_{SW}, the nucleating agent surface accommodates the lattice mismatch of the developing *n*-alkane nuclei through local atomic-scale rearrangement. A softer interface is more conducive to local atomic-scale rearrangement and thus permits the formation of nuclei over a broader range of Δ, reducing τ. For $T = 360$ K and $\lambda_{SW}^* < 0.9$, the nucleating agent melted, so that heterogeneous nucleation could not be observed.
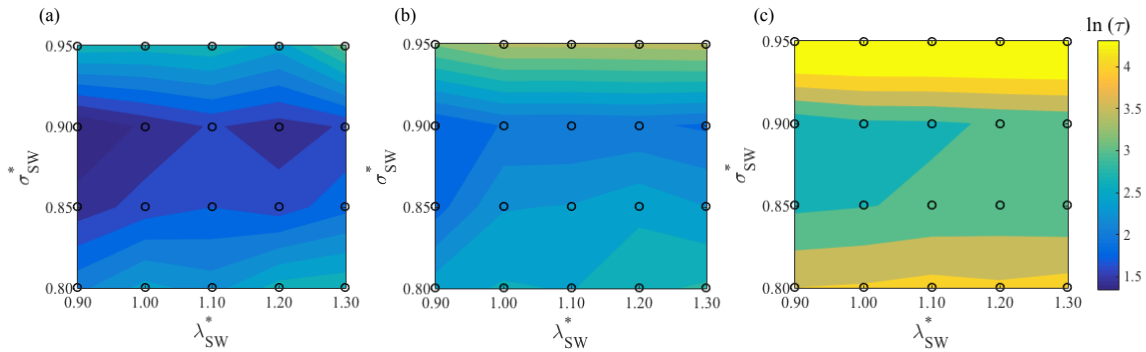

Figure 5. Genomic mapping of induction time to steady-state crystal growth, τ, in C50 for nucleating agents belonging to the tetrahedral crystal family. Induction time is presented as a function of the interatomic distance σ_{SW}^* and tetrahedral strength λ_{SW}^* for three adhesive strengths: (a) $\varepsilon_{AD}^* = 1$, (b) $\varepsilon_{AD}^* = 0.8$ and (c) $\varepsilon_{AD}^* = 0.6$. The (110) crystal plane is exposed to the C50 phase and in all cases, additionally $\varepsilon_{SW}^* = 1$.

The SW parameters ε_{SW} and λ_{SW} have been shown to relate directly to the elastic constants of the crystalline solid.[49] Cowley examined the lattice dynamics for the SW model, and

provided analytical relationships between the SW parameters and the corresponding

stiffness constants C_{11} and C_{44}. Local perturbations around the reference SW values for

silicon show that a 10% increase in C_{11} reflects a ~33% increase in λ_{SW} or a 10% increase

in ε_{SW}. Similarly a 10% increase in C_{44} requires ~14% increase in λ_{SW} or a 10% increase

in ε_{SW}. The elastic properties for a given material in the tetrahedral family can be modeled

by fine adjustment of the two parameters. Thus, elastic stiffness and nucleation efficiency

are parametrically related through λ_{SW}, as shown in Figure 5.

With these heuristics in mind, the computational approach presented here allows one to

search for and design new materials to serve as efficient nucleating agents for *n*-alkanes

and other oligo-ethylenes. Variation of the molecular composition within this class of

tetrahedrally coordinated materials amounts to collective changes in the material

properties that permit reduction in epitaxial mismatch ($|\Delta|$) and/or material rigidity

(C_{11},C_{44}), for example. Examination of data in the literature for materials belonging to the

diamond-like or binary zincblende groups leads to the identification of GaP, AlP, ZnS,

MgS, BeS and BeSe as candidates for heterogeneous nucleation of n-alkanes, based on

the close epitaxial matches in their (110) plane ($|\Delta| \leq 10\%$) and their reasonably low

stiffnesses ($C_{11} \leq 150$ GPa, $C_{44} \leq 70$ GPa).[50] The (111) planes of CdTe and InSb exhibit

somewhat poorer epitaxial match ($|\Delta| \leq 25\%$) but still lower stiffness ($C_{11} \leq 75$ GPa, C_{44}

≤ 30 GPa). The melting and decomposition temperatures of these materials are all well

above the crystallization temperatures for organics, but some (e.g. MgS) may only be

metastable with respect to other polymorphs such as the wurtzite or rock-salt crystal

structures. Others (e.g. AlP) may be unattractive due to their toxicity. Polymorphic

transitions, toxicity and difficulty of particulate dispersion in an organic melt are just a few of the challenges that may yet be encountered when working with these materials in the lab.

Generally speaking, the results presented here expand upon the traditional heuristics used for identification of nucleating agents in crystallizing systems. Not only lattice matching and adhesion strength, but also rigidity of the nucleating agent can serve as a useful property for selecting good nucleating agents in cases such as the one studied here. Careful control over the habit of nucleating agent crystals can provide the means to expose particular crystallographic planes with the desired adhesion strength, lattice spacing and rigidity.[51] Material selection aided by predictive crystal habit models could be used to design and identify nucleating agents with the desired qualities. Chemical modification of the surface of the nucleating agent could be used to boost adhesion strength, offering yet another strategy to improve the nucleating ability of a given crystalline material. Modification of the lattice spacing at the interface would need to be monitored at this stage, as chemical changes could affect the structure of the interface. In this manner, chemical treatment could also be employed as a means to fine-tune lattice periodicity at the surface of the nucleating agent.

Conclusions

In summary, we have demonstrated the systematic study of a family of nucleating agents using molecular dynamics simulation. The representation of the nucleating agent in simulation by a small set of continuously adjustable parameters allows one to define a

materials genome for the nucleating agents, illustrated here for tetrahedrally coordinated crystals. We used the results for crystallization from the melt of long *n*-alkane chains as our measure of nucleating agent efficiency. Relatively poor nucleating agents resulted in long induction times before the steady-state crystal growth rate was observed.

In our parametric scan of nucleating agent properties, we modified the lattice spacing of the crystal unit cell, the lattice rigidity and also the strength of adhesive interactions between the nucleating agent and the n-alkane phase. Results were consistent with heterogeneous nucleation through an epitaxial mechanism: successful matching of the lattice periodicity of the nucleating agent with that of the crystallizing *n*-alkane phase produced a sharp reduction in induction time to crystal growth, but with adhesion strength also playing a role. These observations are consistent with the recent work of Fitzner et al[34] for ice formation on static fcc crystal surfaces. Examination of the first layer of chains deposited atop the nucleating agent surface confirmed that the chain axes align perpendicular to the d_{hkl} spacing of dense, atomic planes along the nucleating agent surface. However, in contrast to Fitzner et al, our study of heterogeneous nucleation using thermalized surfaces allows us to draw conclusions regarding the role of rigidity on nucleating agent efficiency. Reducing the rigidity of the crystal lattice promoted heterogeneous nucleation by broadening the allowance for lattice mismatch. We observed a sharp decrease in τ by increasing the attractive forces between the nucleating agent and the n-alkane. However, there was a limit to this effect, with diminishing gains in τ reduction for an increasingly large magnitude of attraction.

These results show that MD simulation can provide a useful alternative to experiment in the identification of additives for heterogeneous nucleation. Not only can one achieve fine control over all nucleating agent properties and quench conditions, but also, one is able to observe nucleation directly so as to determine the optimum molecular structure for the most efficient nucleating agents. These simulation techniques can be extended to the study of heterogeneous nucleation in a variety of systems including longer chains (e.g. polyethylene), other polymer chemistries and even other non-polymeric systems such as pharmaceuticals, proteins and metals. Likewise, the method is applicable to the study of nucleating agents beyond the tetrahedral crystal system.

References

1. Oxtoby, D.W. Homogeneous nucleation: theory and experiment. *J. Phys. Condens. Matter* **1992**, *4*, 7627–7650.

2. Oxtoby, D.W. Nucleation of first-order phase transitions. *Acc. Chem. Res.* **1998**, *31*, 91-97.

3. Debenedetti, P. G. *Metastable Liquids: Concepts and Principles*; Princeton University Press: Princeton, 1996.

4. Kashchiev, D. *Nucleation: Basic Theory with Applications*; Butterworth-Heinemann: Oxford/Boston, 2000.

5. Price, C. P.; Grzesiak A. L.; Matzger A. J. Crystalline polymorph selection and discovery with polymer heteronuclei. *J. Am. Chem. Soc.* **2005**, *127*, 5512-5517.

6. Abu Baka, M.R.; Nagy, Z. K.; Saleemi, A. N.; Rielly, C. D. The impact of direct nucleation control on crystal size distribution in pharmaceutical crystallization processes. *Cryst. Growth Des.* **2009**, *9*, 1378-1384.

7. Chayen, N. E. Turning protein crystallisation from an art into a science. *Curr. Opin. Struct. Biol.* **2004,** *14*, 577-583.

8. Nanev, C. N. Protein crystal nucleation: recent notions. *Cryst. Res. Technol.* **2006**, *42*, 4-12.

9. Carraher, C. E.; Seymour, R. B. *Polymer Chemistry*; CRC Press: Boca Raton, FL, 2003, pp 44−45.

10. Weissbuch, I.; Addadi, L.; Leiserowitz, L. Molecular recognition at crystal interfaces. *Nature* **1991**, *253*, 637-645.

11. Wittmann, J. C.; Lotz, B. Epitaxial crystallization of polyethylene on organic substrates: a reappraisal of the mode of action of selected nucleating agents. *J. Polym, Sci. B: Polym. Phys.* **1981**, *19*, 1837-1851.

12. Wittmann, J. C.; Hodge, A. M.; Lotz, B. Epitaxial crystallization of polymers onto benzoic acid: polyethylene and paraffins, aliphatic polyesters, and polyamides. *J. Polym, Sci. B: Polym. Phys.* **1983**, *21*, 2495-2509.

13. Binsbergen, F. L. Heterogeneous nucleation in the crystallization of polyolefins: part 1. Chemical and physical nature of nucleating agents. *Polymer* **1970**, *11*, 253-267.

14. Binsbergen, F. L.; de Lange, B. G. M. Heterogeneous nucleation in the crystallization of polyolefins: part 2. Kinetics of crystallization of nucleated polypropylene. *Polymer* **1970**, *11*, 309-322.

15. McPherson, A.; Shlichta, P. Heterogeneous and epitaxial nucleation of protein crystals on mineral surfaces. *Science* **1988**, *239*, 385–387.

16. Chayen, N. E.; Saridakis, E.; Sear, R. P. Experiment and theory for heterogeneous nucleation of protein crystals in a porous medium. *Proc. Natl. Acad. Sci. USA* **2006**, *103*, 597-601.

17. van Duijneveldt, J. S.; Frenkel, D. Computer simulation study of free energy barriers in crystal nucleation. *J. Chem. Phys.* **1992**, *96*, 4655–4668.

18. ten Wolde, P. R.; Ruiz-Montero, M. J.; Frenkel, D. Numerical calculation of the rate of crystal nucleation in a Lennard-Jones system at moderate undercooling. *J. Chem. Phys.* **1996**, *104*, 9932–9947.

19. Auer, S.; Frenkel, D. Prediction of absolute crystal-nucleation rate in hard-sphere colloids. *Nature* **2001**, *409*, 1020–1023.

20. Mandell, M.; McTague, J.; Rahman, A. Crystal nucleation in a three-dimensional Lennard-Jones system: a molecular dynamics study. *J. Chem. Phys.* **1976**, *64*, 3699–3702.

21. Matsumoto, M.; Saito, S.; Ohmine, I. Molecular dynamics simulation of the ice nucleation and growth process leading to water freezing. *Nature* **2002**, *416*, 409–413.

22. Yi, P.; Rutledge, G. C. Molecular simulation of crystal nucleation in n-octane melts. *J. Chem. Phys.* **2009**, *131*, 134902.

23. Yi, P.; Rutledge, G. C. Molecular simulation of bundle-like crystal nucleation from n-eicosane melts. *J. Chem. Phys.* **2011**, *135*, 024903.

24. Yi, P.; Locker, C. R.; Rutledge, G. C. Molecular dynamics simulation of homogeneous crystal nucleation in polyethylene. *Macromolecules* **2013**, *46*, 4723-4733.

25. Salvalaglio, M.; Vetter, T.; Giberti, F.; Mazzotti, M.; Parrinello, M. Uncovering molecular details of urea crystal growth in the presence of additives. *J. Am. Chem. Soc.* **2012**, *134*, 17221-17233.

26. Bourque, A. J.; Locker, C. R.; Rutledge, G. C. Molecular dynamics simulation of surface nucleation during growth of an alkane crystal. *Macromolecules* **2016**, *49*, 3619-3629.

27. Fraux, G.; Doye, J. P. K. Heterogeneous nucleation on silver-iodide like surfaces. *J. Chem. Phys.* **2014**, *141*, 216101.

28. Lupi, L.; Hudait, A.; Molinero, V. Heterogeneous nucleation of ice on carbon surfaces. *J. Am. Chem. Soc.* **2014**, *136*, 3156-3164.

29. Zielke, S. A.; Bertram, A. K.; Patey, G. N. A molecular mechanism of ice nucleation on model AgI surfaces. *J. Phys. Chem. B* **2015**, *119*, 9049-9055.

30. Lupi, L.; Molinero, V. Does hydrophilicity of carbon particles improve their ice nucleation ability? *J. Phys. Chem. A* **2014**, *118*, 7330-7337.

31. Cox, S. J.; Kathmann, S. M.; Slater, B.; Michaelides, A. Molecular simulations of heterogeneous ice nucleation. I. Controlling ice nucleation through surface hydrophobicity. *J. Chem. Phys.* **2015**, *142*, 184704.

32. Cox, S. J.; Kathmann, S. M.; Slater, B.; Michaelides, A. Molecular simulations of heterogeneous ice nucleation. II. Peeling back the layers. *J. Chem. Phys.* **2015**, *142*, 184705.

33. Reinhardt, A.; Doye, J. P K. Effects of surface interactions on heterogeneous ice nucleation for a monatomic water model. *J. Chem. Phys.* **2014**, *141*, 084501.

34. Fitzner, M.; Sosso, G. C.; Cox, S. J.; Michaelides, A. The many faces of heterogeneous ice nucleation: interplay between surface morphology and hydrophobicity. *J. Am. Chem. Soc.* **2015**, 137, 13658-13669.

35. Bourque, A. J.; Rutledge, G. C. Kinetic model for layer-by-layer crystal growth in chain molecules. *Macromolecules* **2016**, *49*, 3656-3964.

36. Stillinger, F. H.; Weber, T. A. Computer simulation of local order in condensed phases of silicon. *Phys. Rev. B* **1985**, *31*, 5262-5271.

37. Palinthrope, B. A. Molecular-dynamics simulation of atomic processes at the low-temperature diamond (111) surface. *J. Appl. Phys.* **1991**, *70*, 543-547.

38. Molinero, V.; Moore, E. B.; Water modeled as an intermediate element between carbon and silicon. *J. Phys. Chem.* **2009,** *113*, 4008-4016.

39. Paul, W.; Yoon, D. Y.; Smith, G. D. An optimized united atom model for simulations of polyethylene melts. *J. Chem. Phys*. **1995**, *103*, 1702−1709.

40. Waheed, N.; Ko, M.; Rutledge, G. C. Molecular simulation of crystal growth in long alkanes. *Polymer* **2005**, *46*, 8689-8702.

41. Waheed, N.; Lavine, M.; Rutledge, G.C. Molecular simulation of crystal growth in n-eicosane. *J. Chem. Phys.* **2002**, *116*, 2301-2309.

42. Plimpton, S. J. Fast parallel algorithms for short-range molecular dynamics. *J. Comput. Phys.* **1995**, *117*, 1-19.

43. Harmandaris, V. A.; Mavrantzas, V. G.; Theodorou, D. N.; Kröger, M.; Ramirez, J.; Öttinger, H. C.; Vlassopoulos, D. Crossover from the Rouse to entangled polymer regime: signals from long, detailed atomistic molecular dynamics simulations, supported by rheological experiments, *Macromolecules* **2003**, *36*, 1376-1387.

44. Julin, J.; Napari, I.; Vehkamäki, H. Comparative study on methodology in molecular dynamics simulation of nucleation. *J. Chem. Phys.* **2007**, *126*, 224517.

45. Chkonia, G.; Wölk, J.; Strey, R.; Wedekind, J.; Reguera, D. Evaluating nucleation rates in direct simulations. *J. Chem. Phys.* **2009**, *130*, 064505.

46. Turnbull, D. Kinetics of heterogeneous nucleation. *J. Chem. Phys.* **1950**, *18*, 198-203.

47. Macrae, C. F.; Edgington, P. R.; McCabe, P.; Pidcock, E.; Shields, G. P.; Taylor, R.; Towler, M.; van de Streek, J. Mercury: visualization and analysis of crystal structures. *J. Appl. Cryst.* **2006**, *39*, 453-457.

48. Turnbull, D.; Vonnegut, B. Nucleation catalysis. *Ind. Eng. Chem.* **1952**, *44*, 1292-1298.

49. Cowley, E. R. Lattice dynamics of silicon with empirical many-body potentials. *Phys. Rev. Lett.* **1988**, *60*, 2379-2381.

50. Adachi, S. *Properties of Semiconductor Alloys: Group-IV, III-V and II-VI Semiconductors*; John Wiley & Sons Ltd: West Sussex, UK, 2009.

51. Mullin, J. W. *Crystallization*; Butterworth-Heinemann: Oxford/Boston, 1961.

TOC Graphic